THE JOURNAL OF PHYSICAL CHEMISTRY C
A JOURNAL OF THE AMERICAN CHEMICAL SOCIETY

pubs.acs.org/JPCC

Article

Enhancing Photoelectrochemical Performance of Sb_2S_3 through Single-Crystal Growth on Ni-Coated FTO Substrates

Mao Zhang,* Wonjung Park, Yeojin Kang, Ramesh Kumar Chitumalla, Tae-Hoon Kim, Joonkyung Jang, and Dongyun Lee*

Cite This: *J. Phys. Chem. C* 2024, 128, 17463−17469

Read Online

ACCESS | Metrics & More | Article Recommendations | Supporting Information

ABSTRACT: Sb_2S_3 is a binary compound semiconductor composed of elements that have a large absorption coefficient of solar energy and are relatively abundant on Earth, and it has recently spurred great interest as a promising light-absorbing material for solar energy conversion. Sb_2S_3 consists of one-dimensional (1-D) covalently linked nanoribbons stacked via van der Waals forces. Therefore, one-dimensional (1-D) Sb_2S_3 single crystals can be synthesized by adjusting the experimental conditions. However, most of these studies focused on hydrothermal methods, and it took more than 10 h to prepare a one-dimensional Sb_2S_3 single crystal. In this study, a novel approach is presented to fabricate single-crystal Sb_2S_3 pillars by spin coating Sb_2S_3 precursor solution on Au- and Ni-coated FTO glasses with significantly enhanced photoelectrochemical performance compared to Sb_2S_3 prepared on bare FTO glass and Mo-coated FTO glass.

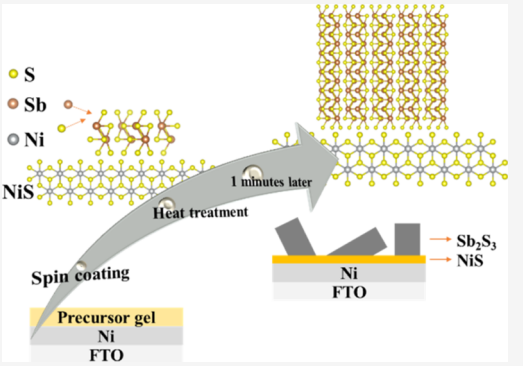

1. INTRODUCTION

Hydrogen is emerging as a crucial, clean alternative to fossil fuels due to its high energy density and the ability to produce it through sustainable methods like photoelectrochemical (PEC) water splitting, which uses semiconductors to convert sunlight directly into energy.[1,2] In this process, the oxygen evolution reaction (OER) occurs at the anode and the hydrogen evolution reaction (HER) occurs at the cathode, splitting water into hydrogen and oxygen with a required potential of 1.23 V per electron, corresponding to 237.2 kJ/mol under standard conditions, and necessitating a semiconductor band gap over 1.23 eV.[3−5] Antimony sulfide (Sb_2S_3), with its ideal band gap of 1.5−1.8 eV and high light absorption, is considered a promising material for PEC, particularly as a photoanode.[6−8,18] While Sb_2S_3 has been studied extensively in the photovoltaic (PV) industry, its application in PEC is less explored, though it is known to potentially achieve a peak photocurrent density of about 24.5 mA·cm^{-2} under simulated sunlight, translating to a solar-to-hydrogen efficiency of 28%.[9−18] Despite this potential, actual studies often report lower efficiencies, suggesting a need for further research into improving the material's properties, such as its tendency to form polycrystalline structures that hinder performance due to grain boundaries, which act as charge traps.[19] Research also suggests potential in using one-dimensional single crystals of Sb_2S_3 that exhibit strong covalent bonds and could enhance PEC performance, though these structures are complex to produce and remain under-researched.[20−34]

In this study, we focus on assessing the photoelectrochemical (PEC) properties of single-crystal Sb_2S_3 synthesized on Ni-coated FTO glass, a continuation of our work on rapid sol−gel processes suitable for photoelectrode fabrication.[35,36] We aim to understand the enhancement in photoelectric conversion characteristics provided by Ni coating compared with bare FTO glass and Mo-coated FTO glass. To achieve this, we conducted PEC tests on pure Sb_2S_3 without additional catalysts, exploring the intrinsic capabilities of the material.

2. EXPERIMENTAL PROCEDURE

To investigate the growth process of Sb_2S_3 on Ni-coated FTO glass, we employed transmission electron microscopy (TEM, TALOS F200X model, FEI). The sample preparation was carried out with a focused ion beam (FIB, Scios, FEI), which included a microsampling system. Additionally, periodic density functional theory (DFT) simulations were conducted to support the experimental findings concerning Sb_2S_3 crystal growth on the Ni-coated substrate. These simulations were validated by comparing them with experimental data from X-ray diffraction (XRD, Cu−Kα radiation (λ = 1.5418 Å),

Received: August 19, 2024
Revised: September 25, 2024
Accepted: September 26, 2024
Published: October 2, 2024

https://doi.org/10.1021/acs.jpcc.4c05586
J. Phys. Chem. C 2024, 128, 17463−17469

X'pert,[3] Malvern Panalytical, U.K.) patterns. Details of the simulation process are included in the Supporting Information.

The synthesis of the Sb_2S_3 structure involved dissolving antimony(III) chloride ($SbCl_3$) and thiourea (TU) in methyl alcohol (2-ME), and this solution was then spin-coated onto various substrates including plain FTO glass as well as FTO glass coated with Au, Ni, and Mo. An extensive description of the synthesis procedure can be found in previous studies.[35,36] Additionally, the structural analysis techniques employed, including scanning electron microscopy (SEM, SUPRA25, Zeiss, Germany), are detailed in earlier research. For this study, Raman spectroscopy (UniRAM, Uninanotech, Korea) was also performed to identify the predominant bonds in the Sb_2S_3 structure when formed on different substrates.

The photoelectrochemical (PEC) properties of the Sb_2S_3-based pillar structure photoanodes were characterized by using a three-electrode configuration in an electrochemical workstation (IviumStat, Ivium Tech, Netherlands). The working electrode comprised the Sb_2S_3 photoanodes, while a saturated Ag/AgCl/KCl electrode and a Pt mesh served as the reference and counter electrodes, respectively. Nonessential areas of the electrode were coated with silicone gel. PEC measurements were taken in a 0.1 M Na_2SO_4 solution under one sun illumination condition. All potentials applied during the experiments were referenced to the reversible hydrogen electrode (RHE) scale, allowing for comparison with previous reports. The conversion of potential followed the equation:

$$E_{RHE} = E_{Ag/AgCl} + 0.059\,pH + 0.197 \quad (1)$$

Linear sweep voltammetry was conducted at a scan rate of 5 $mV{\cdot}s^{-1}$, and electrochemical impedance spectra were recorded over a frequency range from 0.1 Hz to 100 kHz with a signal amplitude of 10 mV.

3. RESULTS AND DISCUSSION

3.1. Microstructures of Sb_2S_3. X-ray diffraction analysis was performed on Sb_2S_3 fabricated on Ni-coated FTO glass, and bare FTO and Au-coated FTO glass substrates were used for comparison (Figure 1). It revealed predominant peaks consistent with stibnite Sb_2S_3 (JCPDS No.42−1393, space group *Pnma*; a = 11.3110 Å; b = 3.8390 Å; c = 11.2230 Å and $\alpha = \beta = \gamma = 90°$) while peaks indicative of Au-based compounds were negligible. For the Sb_2S_3 grown on Ni-coated FTO glass, there are indications of NiS peaks, which probably form around 160 °C.[35,37] The XRD patterns shown in Figures 1a (top) and S6(b) present peaks corresponding to NiS crystals at the (100), (101), (102), and (110) indices, approximately at 30.18, 34.73, 45.86, and 53.55° of 2-θ, as cited in JCPDS 01−075−0613. Figure 1b depicts a schematic of the NiS crystal structure, emphasizing the (100), (101), (102), and (110) planes. Definitely, the XRD patterns imply the successful creation of crystalline Sb_2S_3 via the sol−gel process, and the substrates have a great influence on the orientation of Sb_2S_3. As mentioned before,[35] the (020) peak intensity of Sb_2S_3 prepared on bare FTO can be decreased by Ni doping. In addition, for Sb_2S_3 prepared on Au-coated FTO glass,[36] the (020) peak intensity of Sb_2S_3 prepared can be decreased and Sb_2S_3 single crystal can be formed because of the $AuSb_2$ formed between the interface of Au and Sb_2S_3. Further analysis of the formation mechanism is listed in the following part.

Raman spectral validation confirmed similar results for Sb_2S_3 on bare FTO, Au-, and Ni-coated FTO glasses as shown in Figure 2. The bands identified correspond to various bonds in the compound, with some attributed to laser-induced phase transformations (Figure S1).[38−40] Interestingly, Sb_2S_3 on Au-, Ni-coated substrates exhibited pillar formation and short square-shaped growth on bare FTO glass showed, while film-type with cracks and organic residue was observed on Mo-coated substrate reported in previous studies.[35,36]

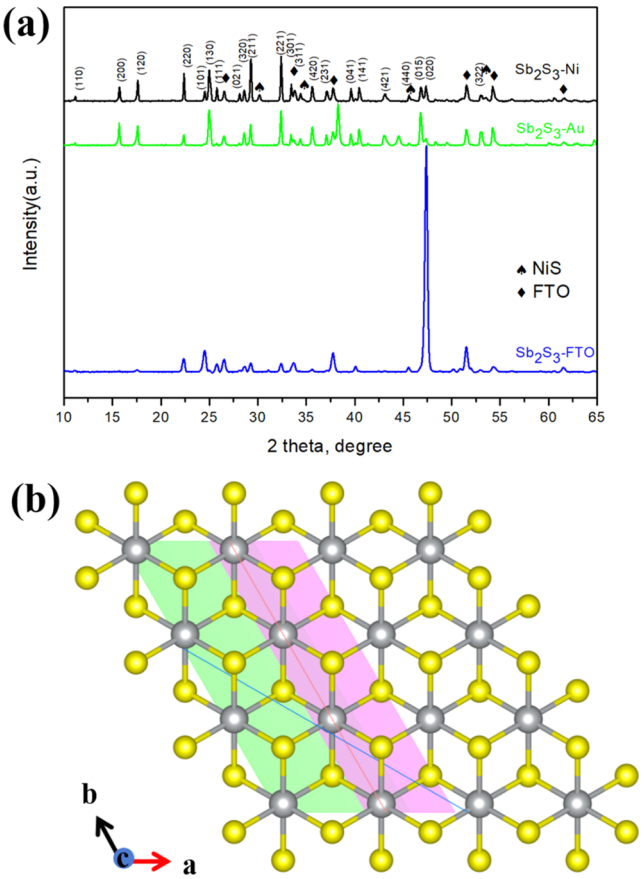

Figure 1. (a) X-ray diffraction patterns of Sb_2S_3 prepared on bare FTO, Au-, and Ni-coated FTO glasses, respectively note: small nonindexed peaks are all Sb_2S_3 peaks and (b) crystal structure of NiS(3 × 3 × 3) marked with (100) (red), (101) (green), (102) (magenta), and (110) (blue) planes (the yellow ball represents S, and the gray ball represents Ni).

Based on phase diagrams[41] and previous studies,[35,36] we infer that NiS and $AuSb_2$ play roles in the pillar structure formation at temperatures under 160 °C. This process is supported by energy-dispersive X-ray spectroscopy (EDS, Xplore, Oxford Instruments, U.K.) analysis (Figure S2) of Sb_2S_3 on Ni-coated FTO glass, which revealed an S/Sb ratio of 1.3, with 3.8 atomic % O. Thus, it is clear that high-quality crystalline Sb_2S_3 can be synthesized on bare and Au-, Ni-coated FTO glass substrates, though Mo-coated samples exhibit signs of organic impurities.

A TEM analysis was conducted to examine the microstructure of the Sb_2S_3 pillars that developed on the Ni-coated FTO glass substrate. This was done to gain insight into the growth mechanism of the Sb_2S_3 pillar structure. Note that TEM analysis of Sb_2S_3 grown on Au-coated FTO substrate was previously discussed in ref 36. Figure S3 offers a close-up TEM image of the junction between the Sb_2S_3 pillar and the substrate. From the EDS elemental mapping images (as seen in Figure S4(a,d)) and XRD patterns, we identified the formation

https://doi.org/10.1021/acs.jpcc.4c05586
J. Phys. Chem. C 2024, 128, 17463−17469

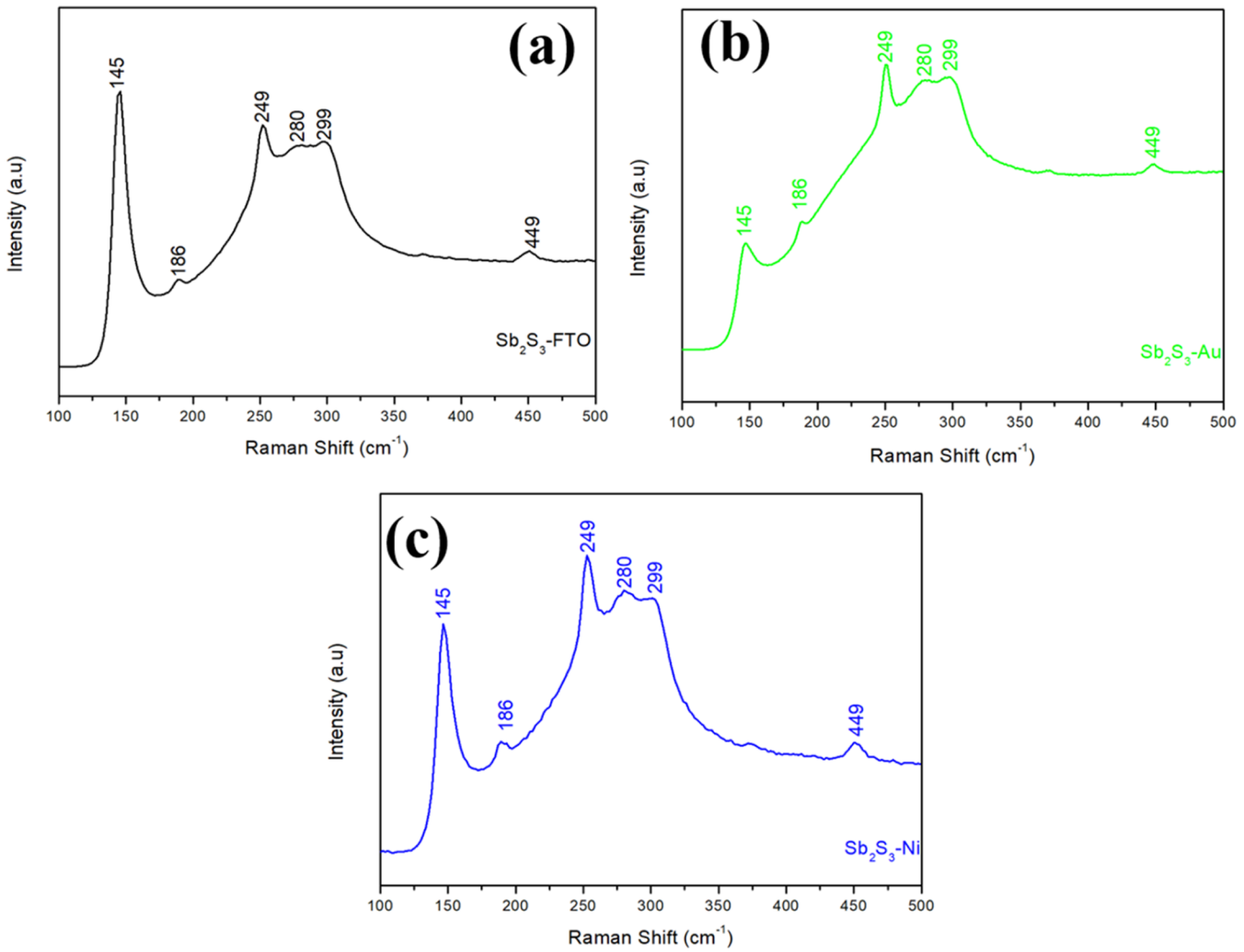

Figure 2. Raman spectra of Sb_2S_3. (a–c) Raman spectra of Sb_2S_3 prepared on bare FTO, Au-, and Ni-coated FTO glasses.

of a NiS layer between the Ni-coating layer and the Sb_2S_3 pillar. Referring to prior studies,[35−37] the NiS layer tends to form first during the specimen's heat treatment process due to its lower formation temperature compared to Sb_2S_3. Subsequently, the Sb_2S_3 pillar develops on top of the NiS layer. In order to further prove the importance of NiS, Sb_2S_3 precursor solution was also prepared on the NiS substrate under the same condition as Sb_2S_3 prepared on FTO, Au-, and Ni-coated FTO glasses. The NiS substrate was prepared by spin coating 0.6 M thiourea solution on the Ni-coated FTO glass, and the heat-treated under the same conditions as the preparation conditions of Sb_2S_3. As shown in Figures S6−S8, the Sb_2S_3 pillar has been successfully fabricated on the NiS substrate. Figure 3a−d unambiguously shows the emergence of single-crystal Sb_2S_3 pillars. Additionally, the crystal presumed to be the NiS layer displayed consistent crystallinity with minimal defects.

The fast Fourier transform (FFT) and SAED patterns for Sb_2S_3 pillars both exhibit single-crystal orthorhombic diffraction patterns aligned with the $[\bar{1}01]$ zone axis.[35,36] While some pillars orient in slightly varying directions, all Sb_2S_3 pillars appear to grow in the [111] direction. Figure 3e,f details the positioning of the (111) and (010) planes in the crystal, where Sb_2S_3 pillars develop and offer a schematic representation of their growth trajectory, respectively. It is worth noting that HRTEM and FFT analyses were similarly conducted on slightly different positions (segments) of the interface between the Sb_2S_3 pillars and NiS, and despite the variation in location, comparable results were obtained, as shown in Figure S8. This suggests that the sample exhibits consistent characteristics across different regions.

As previously mentioned, Sb_2S_3 is capable of forming single-crystal rods through hydrothermal methods without needing a substrate, but this requires higher temperatures and extended annealing times compared to our method. When Sb_2S_3 is prepared on both bare FTO glass and Mo-coated FTO glass under identical conditions, it exhibits polycrystalline properties. This indicates that NiS plays a significant role in the creation of Sb_2S_3 single-crystal pillars, akin to how $AuSb_2$ forms on Au-coated substrates. Jing and colleagues demonstrated that orthorhombic Sb_2S_3 can consistently grow vertically from a CdS layer by establishing two coordination bonds, namely $S_{(Sb_2S_3)}-Cd_{(CdS)}$ and $Sb_{(Sb_2S_3)}-S_{(CdS)}$, with a moderate gradient. There have been accounts of $(Sb_4S_6)n$ ribbons readily expanding in the [001] direction as the reaction progressed from the initial atomic stage.

In a similar vein, Sb_2S_3 secures the initial Sb and S atoms by creating $S_{(Sb_2S_3)}-Ni_{(NiS)}$ and $Sb_{(Sb_2S_3)}-S_{(NiS)}$ auxiliary bonds. This then leads to the formation of single-crystal pillars on NiS

https://doi.org/10.1021/acs.jpcc.4c05586
J. Phys. Chem. C 2024, 128, 17463−17469

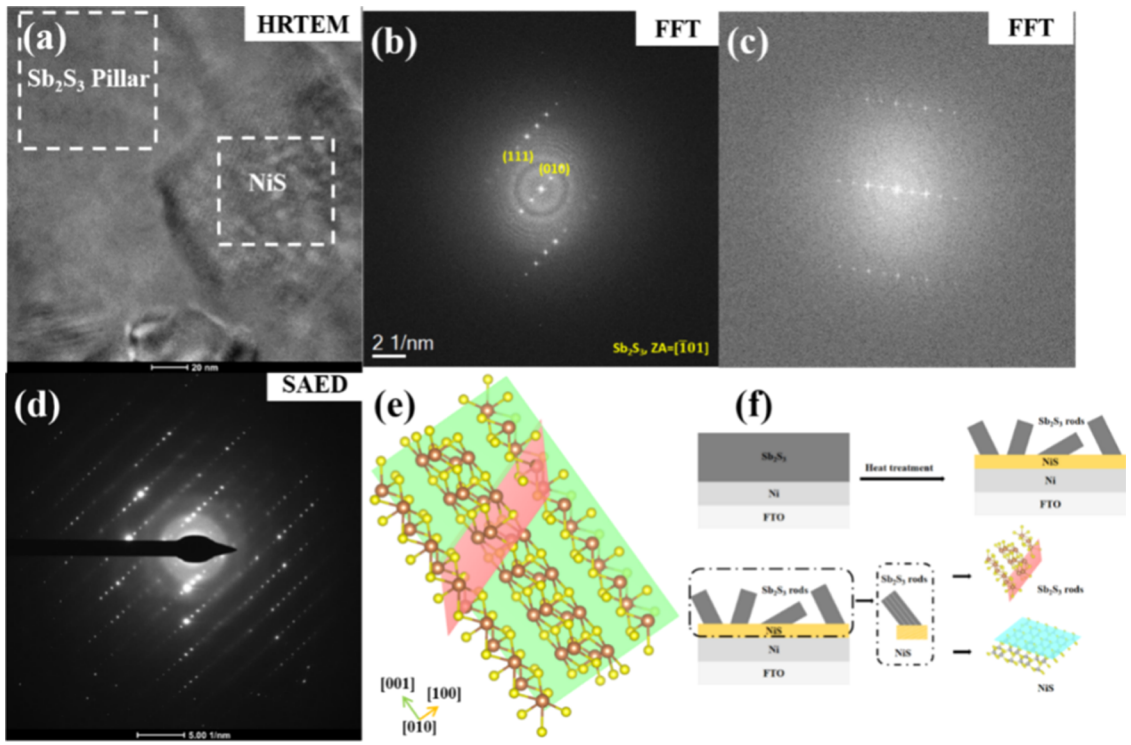

Figure 3. Sb_2S_3 pillar prepared on Ni-coated FTO glass with spin coating and heat treatment for 6 times. (a) High-resolution TEM (HRTEM) image; (b) fast Fourier transform (FET) image of Sb_2S_3 pillar; (c) fast Fourier transform (FET) image of NiS; (d) selected-area electron diffraction (SAED) of Sb_2S_3 pillar; (e) crystal structure of Sb_2S_3 marked with (111) (red) and (010) (green) planes (the yellow ball represents S, and the wine ball represents Sb); and (f) formation process of Sb_2S_3 single-crystal rods.

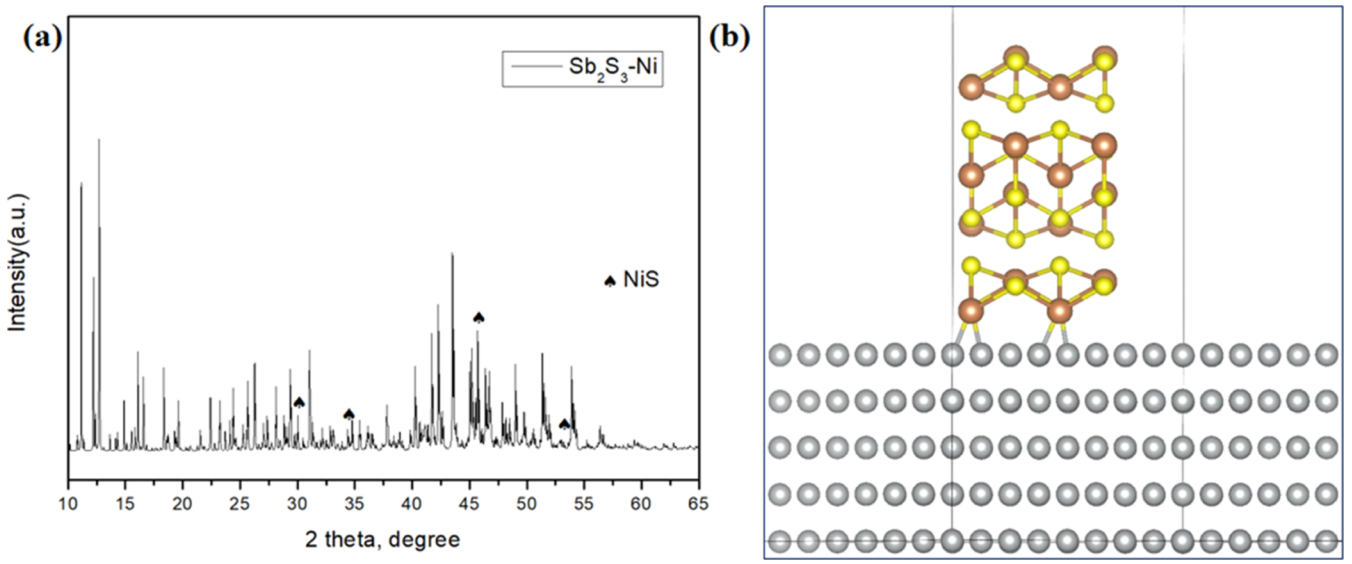

Figure 4. (a) Simulated X-ray diffraction pattern of one-dimensional Sb_2S_3 single-crystal growth on Ni(111) surface; (b) simulated atomistic model of 1-dimensional crystal growth of Sb_2S_3 on Ni(111) substrate. The Sb_2S_3 ribbons are vertically oriented on the nickel surface. Nickel (Ni), sulfur (S), and antimony (Sb) atoms are represented by silver, yellow, and brown spheres, respectively.

through the generation of Sb_2S_3 ions, singular bonds. The comprehensive process of Sb_2S_3 pillar formation is illustrated in Figure 3f. In order to further clarify the Sb_2S_3 single-crystal growth on the Ni substrate, DFT simulations were performed. As shown in Figure S6, Ni-coated FTO glass shows a preferred orientation on (111), so Sb_2S_3 ribbons and a Ni (111) plane were chosen to create the atomistic model (Figure S9). Considering the combination between the $(Sb_4S_6)_n$ ribbon and the substrate surface, we calculated the atom displacement distributions using the Vienna ab initio Simulation Package (VASP). The calculated results show that the Sb_4S_6 unit standing vertically on the Ni (111) plane is stable with lower distortion (Figure 4b), and the corresponding simulated X-ray diffraction pattern is shown in Figure 4a. NiS can form between the interface of the Sb_2S_3 ribbons and Ni.

3.2. Photoelectrochemical Properties of Sb_2S_3. The photoelectrical properties of Sb_2S_3 thin films were characterized by measuring photocurrent. Transient photocurrent

https://doi.org/10.1021/acs.jpcc.4c05586
J. Phys. Chem. C 2024, 128, 17463−17469

density of Sb_2S_3 prepared on bare FTO, Au-, and Ni-coated FTO glasses with chopped light illumination at 0 (Figure S10(a)) and 0.62 V (Figure S10(b), 0.62 V vs Ag/AgCl equals 1.23 V vs RHE) bias voltage is shown in Figure S6. All samples exhibit a fast light response. Under illumination, all transient photocurrents featured a sharp anodic rise followed by an exponential decay, known as a spike. The existence of spikes is associated with the occurrence of the electron−hole recombination process at the semiconductor surface, which can be observed in a variety of semiconductor materials.[42]

The photocurrent of Sb_2S_3 is mainly determined by the photogenerated hole transfer efficiency in Sb_2S_3 (working electrode)/electrolyte and electron diffusion into the back contact. In this research, the OER took place at the Sb_2S_3 working electrode, while HER took place at the Pt mesh counter electrode. Electrons and holes contribute to the photocurrent and lead to low resistance in the illuminated state, so when the light is blocked, the current momentarily drops below the initial value in the dark and then recovers.[43,44] As noted in Figure S10(a), Sb_2S_3 prepared on Ni-coated FTO glass displays the highest transient photocurrent current of 91.98 $\mu A \cdot cm^{-2}$, while the transient photocurrent of Sb_2S_3 prepared on Au-coated FTO glass and bare FTO glass is 65.12 and 15.93 $\mu A \cdot cm^{-2}$, respectively. By applying a 0.62 V vs Ag/AgCl, a larger transient photocurrent was observed, 175.37 $\mu A \cdot cm^{-2}$ for Sb_2S_3 prepared on Ni-coated FTO glass, 171.94 $\mu A \cdot cm^{-2}$ for Sb_2S_3 prepared on Au-coated FTO glass, and 22.70 $\mu A \cdot cm^{-2}$ for Sb_2S_3 prepared on bare FTO glass.

The PEC properties were estimated by linear sweep voltammetry (LSV), which assists in evaluating the fundamental properties of a photoelectrode, such as its potential for photocurrent onset as well as its ability to generate photocurrent at a given potential. Figure 5a shows the PEC behaviors of Sb_2S_3 prepared on bare FTO glass and Au- and Ni-coated FTO glasses. The photocurrent densities gradually increased with the applied bias increasing, meaning the improved electron−hole pairs separation and transfer efficiency. Sb_2S_3 prepared on Au- and Ni-coated FTO glasses exhibited a much larger photocurrent density than Sb_2S_3 prepared on bare FTO glass, and the corresponding photocurrent density at 1.23 V vs RHE is 281.84, 321.901, and 124.66 $\mu A \cdot cm^{-2}$, separately (Figure S11). Based on the above discussion, Sb_2S_3 prepared on Au- and Ni-coated FTO glasses with pillar structures has a much better performance than Sb_2S_3 prepared on bare FTO glass and Mo-coated FTO glass, and Sb_2S_3 prepared on Ni-coated FTO glass has the best performance because NiS can be used as the catalyst for water splitting.[18,45] As shown in previous research,[35] Sb_2S_3 with the pillar structure has the same band gap value of 1.5 eV as that of Sb_2S_3 prepared on bare FTO glass, so this is not the reason for the improvement of the performance, and it should be attributed to the fine single-crystal structure of Sb_2S_3 prepared on Au- and Ni-coated FTO glasses.

Electrochemical impedance spectroscopy (EIS) was also conducted to investigate the charge transfer kinetics of Sb_2S_3 prepared on bare FTO glass and Ni-coated FTO glass, and the resulting Nyquist plots are shown in Figure 5b. It is evident that the impedance arc of Sb_2S_3 prepared on Ni-coated FTO glass is much smaller than that of Sb_2S_3 prepared on bare FTO glass, indicating a lower charge transfer resistance and therefore enhanced charge transfer capability of Sb_2S_3 prepared on Ni-coated FTO glass. Based on the EIS results, as seen in Figure 5a, it can be inferred that the improved photoelectric

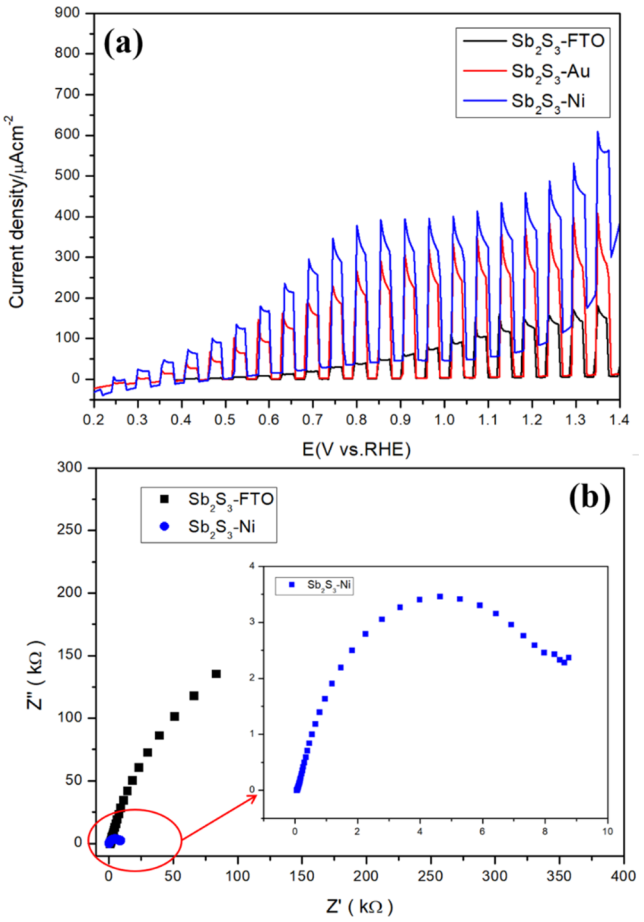

Figure 5. Photoelectrochemical properties of Sb_2S_3 prepared on bare FTO, Au-, Ni-coated FTO glasses: (a) Current density-potential plots; (b) EIS plots of Sb_2S_3 prepared on bare FTO and Ni-coated FTO glasses.

conversion efficiency of the Sb_2S_3−Ni sample, compared to the other specimens, is partially due to this. However, a more detailed analysis is required to fully understand how Ni coating specifically influences photoelectric conversion.

4. CONCLUSIONS

This study examined the microstructures and photoelectrical properties of Sb_2S_3, highlighting the influence of the substrate material on these characteristics. The microstructural analysis, using XRD, Raman spectroscopy, and SEM, confirmed the successful synthesis of crystalline Sb_2S_3 on various substrate materials. However, Ni-coated substrates showed signs of NiS compound formation, likely due to interactions occurring at elevated temperatures. Morphologically, substrate influence was also suggested, with distinctive square-shaped growth on bare FTO glass and pillar structures on Au and Ni-coated substrates. Interestingly, the Mo-coated substrate showed signs of organic impurities, possibly residual from the precursor materials.

During photoelectrical characterizations, transient photocurrent density measurements demonstrated rapid light responses from all samples, with spikes indicating the electron−hole recombination process. Importantly, Sb_2S_3 on Ni-coated FTO glass exhibited the highest photocurrent densities, implying more efficient photogenerated hole transfer and electron diffusion. Sb_2S_3 prepared on a Mo-coated

https://doi.org/10.1021/acs.jpcc.4c05586
J. Phys. Chem. C 2024, 128, 17463−17469

substrate showed negligible photocurrent, likely due to residual organic impurities affecting the photophysical properties.

Further PEC analysis corroborated these findings, showing increased photocurrent densities with a increased bias for Sb_2S_3 on Au- and Ni-coated substrates, with the Ni-coated samples performing best. The superior performance of the Ni-coated substrate sample was further validated by EIS analysis, which revealed a lower charge transfer resistance, indicating an enhanced charge transfer ability.

Our findings highlight that while Sb_2S_3 can be successfully synthesized on various substrates, substrate choice significantly influences the resulting microstructures and photoelectrical properties. More specifically, Sb_2S_3 fabricated on Ni-coated FTO glass delivers the best photoelectrical performance due to optimal morphology and charge transfer efficiency. These insights could prove valuable for optimizing Sb_2S_3-based device performance in solar and other photoelectrical applications. Future work could explore additional substrate material combinations and investigate the potential of engineering more efficient microstructures.

■ ASSOCIATED CONTENT

Supporting Information

The Supporting Information is available free of charge at https://pubs.acs.org/doi/10.1021/acs.jpcc.4c05586.

Raman spectra & TEM images; EDS spectra; XRD patterns; simulation results; photocurrent density; and PEC measurement (PDF)

■ AUTHOR INFORMATION

Corresponding Authors

Mao Zhang − *Department of Nano Fusion Technology, Pusan National University, Busan 46241, Republic of Korea*; Email: zhangmao7412@gmail.com

Dongyun Lee − *Department of Nano Fusion Technology, Pusan National University, Busan 46241, Republic of Korea; Department of Nanoenergy Engineering, Pusan National University, Busan 46241, Republic of Korea*; orcid.org/0000-0003-1941-4708; Email: dlee@pusan.ac.kr

Authors

Wonjung Park − *Department of Nano Fusion Technology, Pusan National University, Busan 46241, Republic of Korea*; Present Address: KSTE, 10−38, Dongtansandan 5-gil, Hwaseong-si, Gyeonggi-do 18487, Republic of Korea

Yeojin Kang − *Department of Nano Fusion Technology, Pusan National University, Busan 46241, Republic of Korea*; Present Address: Samsung Electro-Mechanics, 150, Maeyeong-ro, Yeongtong-gu, Suwon-si, Gyeonggi-do 16674, Republic of Korea

Ramesh Kumar Chitumalla − *Department of Nano Fusion Technology, Pusan National University, Busan 46241, Republic of Korea*; orcid.org/0000-0002-9523-7056

Tae-Hoon Kim − *Department of Materials Science & Engineering, Chonnam National University, Gwangju 61186, Republic of Korea*; orcid.org/0000-0002-3505-4899

Joonkyung Jang − *Department of Nano Fusion Technology, Pusan National University, Busan 46241, Republic of Korea; Department of Nanoenergy Engineering, Pusan National University, Busan 46241, Republic of Korea*; orcid.org/0000-0001-9028-0605

Complete contact information is available at: https://pubs.acs.org/10.1021/acs.jpcc.4c05586

Notes

The authors declare no competing financial interest.

■ ACKNOWLEDGMENTS

This research was funded by the National Research Foundation of Korea (NRF) funded by the Ministry of Science and ICT (No. 2021R1F1A1054803).

■ REFERENCES

(1) Turner, J. A. A Realizable Renewable Energy Future. *Science* **1999**, *285*, 687−689.

(2) Lubitz, W.; Tumas, W. Hydrogen: an overview. *Chem. Rev.* **2007**, *107*, 3900−3903.

(3) Ros, C.; Teresa, A.; Morante, J. R. Photoelectrochemical water splitting: a road from stable metal oxides to protected thin film solar cells. *J. Mater. Chem. A* **2020**, *8*, 10625−10669.

(4) Bard, A. J.; Fox, M. A. Artificial photosynthesis: solar splitting of water to hydrogen and oxygen. *Acc. Chem. Res.* **1995**, *28*, 141−145.

(5) Walter, M. G.; Warren, E. L.; McKone, J. R.; Boettcher, S. W.; Mi, Q.; Santori, E. A.; Lewis, N. S. Solar water splitting cells. *Chem. Rev.* **2010**, *110*, 6446−6473.

(6) Kondrotas, R.; Chen, C.; Tang, J. Sb_2S_3 solar cells. *Joule* **2018**, *2*, 857−878.

(7) Perales, F.; Lifante, G.; Agullo-Rueda, F.; Heras, C. Optical and structural properties in the amorphous to polycrystalline transition in Sb_2S_3 thin films. *J. Phys. D: Appl. Phys.* **2007**, *40*, 2440−2444.

(8) Salem, A. M.; Selim, M. S.; Salem, A. M. Structure and optical properties of chemically deposited Sb_2S_3 thin films. *J. Phys. D: Appl. Phys.* **2001**, *34*, 12−17.

(9) Prabhakar, R. R.; Moehl, T.; Siol, S.; Suh, J.; Tilley, S. D. Sb_2S_3/TiO_2 heterojunction photocathodes: band alignment and water splitting properties. *Chem. Mater.* **2020**, *32*, 7247−7253.

(10) de Araújo, M. A.; Mascaro, L. H. Plasma Treatment: a Novel Approach to Improve the Photoelectroactivity of Sb_2S_3 Thin Films to Water Splitting. *ChemElectroChem* **2020**, *7*, 2325−2329.

(11) Wang, Z.; Li, L.; Hong, L.; Shi, X.; Lu, Y.; Su, J. Bi Doped Sb_2S_3 Thin Film Synthesized by a Two-Step Approach with Enhanced Photoelectrochemical Water Splitting Performance. *J. Electrochem. Soc.* **2022**, *169*, No. 066508.

(12) Zhao, J.; Cheng, Y.; Chen, Y.; Zhang, W.; Liu, E.; Fan, J.; Miao, H.; Hu, X. Defects regulation of Sb_2S_3 by construction of Sb_2S_3/In_2S_3 direct Z-scheme heterojunction with enhanced photoelectrochemical performance. *Appl. Surf. Sci.* **2021**, *568*, No. 150917.

(13) Liang, Y.; Wang, J.; Liu, F.; Jia, M.; Jiang, L. Construction of PANI/Sb_2S_3 p−n junction photoanode for enhancing photoelectrochemical water oxidation. *J. Electrochem. Soc.* **2021**, *168*, No. 066512.

(14) DeAngelis, A. D.; Kemp, K. C.; Gaillard, N.; Kim, K. S. Antimony (III) sulfide thin films as a photoanode material in photocatalytic water splitting. *ACS Appl. Mater. Interfaces* **2016**, *8*, 8445−8451.

(15) Wang, L.; Lian, W.; Liu, B.; Lv, H.; Zhang, Y.; Wu, X.; Wang, T.; Gong, J.; Chen, T.; Xu, H. A Transparent, High-Performance, and Stable Sb_2S_3 Photoanode Enabled by Heterojunction Engineering with Conjugated Polycarbazole Frameworks for Unbiased Photoelectrochemical Overall Water Splitting Devices. *Adv. Mater.* **2022**, *34*, No. 2200723.

(16) de Araújo, M. A.; Costa, M. B.; Mascaro, L. H. Improved Photoelectrochemical Hydrogen Gas Generation on Sb_2S_3 Films Modified with an Earth-Abundant MoS_x Co-Catalyst. *ACS Appl. Energy Mater.* **2022**, *5*, 1010−1022.

(17) de Araújo, M. A.; Lucas, F. W. S.; Mascaro, L. H. Effect of the electrodeposition potential on the photoelectroactivity of the SnS/Sb_2S_3 thin films. *J. Solid State Electrochem.* **2020**, *24*, 389−399.

(18) Chen, Z.; Dinh, H. N.; Miller, E. *Photoelectrochemical Water Splitting: Standards, Experimental Methods, and Protocols*; Springer: New York, 2013.
(19) Cheng, X.; Yang, S.; Cao, B.; Tao, X.; Chen, Z. Single crystal perovskite solar cells: development and perspectives. *Adv. Funct. Mater.* **2020**, *30*, No. 1905021.
(20) Yang, J.; Liu, Y. C.; Lin, H. M.; Chen, C. C. A chain-structure nanotube: growth and characterization of single-crystal Sb_2S_3 nanotubes via a chemical vapor transport reaction. *Adv. Mater.* **2004**, *16*, 713−716.
(21) Li, C.; Yang, X.; Liu, Y.; Zhao, Z.; Qian, Y. Growth of crystalline Sb_2S_3 nanorods by hydrothermal method. *J. Cryst. Growth* **2003**, *255*, 342−347.
(22) Qiao, J.; Zhang, X.; Liu, C.; Wang, Z.; Liu, W.; Wang, F.; Liu, J. High-permittivity Sb_2S_3 single-crystal nanorods as a brand-new choice for electromagnetic wave absorption. *Sci. China Mater.* **2021**, *64*, 1733−1741.
(23) Zhang, J.; Hou, K.; Huang, T.; Yang, J.; Xu, B.; Li, S.; Yang, B.; Ma, W. Single-Crystal Sb_2S_3 Tube Prepared by Chemical Vapor Deposition for a 1 cm Photodetector Application. *ACS Appl. Electron. Mater.* **2022**, *4*, 2455−2462.
(24) Varghese, J.; Barth, S.; Keeney, L.; Whatmore, R. W.; Holmes, J. D. Nanoscale ferroelectric and piezoelectric properties of Sb_2S_3 nanowire arrays. *Nano Lett.* **2012**, *12*, 868−872.
(25) Yu, Y.; Wang, R. H.; Chen, Q.; Peng, L. M. High-quality ultralong Sb_2S_3 nanoribbons on large scale. *J. Phys. Chem. B* **2005**, *109*, 23312−23315.
(26) Cheng, Y.; Yao, Z.; Zhang, Q.; Chen, J.; Ye, W.; Zhou, S.; Liu, H.; Wang, M. S. In situ atomic-scale observation of reversible potassium storage in Sb_2S_3 @ carbon nanowire anodes. *Adv. Funct. Mater.* **2020**, *30*, No. 2005417.
(27) Lou, W.; Chen, M.; Wang, X.; Liu, W. Novel single-source precursors approach to prepare highly uniform Bi_2S_3 and Sb_2S_3 nanorods via a solvothermal treatment. *Chem. Mater.* **2007**, *19*, 872−878.
(28) Salinas-Estevané, P.; Sanchez, E. M. Preparation of Sb_2S_3 nanostructures by the ionic liquid-assisted sonochemical method. *Cryst. Growth Des.* **2010**, *10*, 3917−3924.
(29) Chen, G.-Y.; Zhang, W.; Xu, A. Synthesis and characterization of single-crystal Sb_2S_3 nanotubes via an EDTA-assisted hydrothermal route. *Mater. Chem. Phys.* **2010**, *123*, 236−240.
(30) Geng, Z. R.; Wang, M. X.; Yue, G. H.; Yan, P. X. Growth of single-crystal Sb_2S_3 nanowires via solvothermal route. *J. Cryst. Growth* **2008**, *310*, 341−344.
(31) Hu, H.; Liu, Z.; Yang, B.; Mo, M.; Li, Q.; Yu, W.; Qian, Y. Solvothermal growth of Sb_2S_3 microcrystallites with novel morphologies. *J. Cryst. Growth* **2004**, *262*, 375−382.
(32) Mo, M.; Zhu, Z.; Yang, X.; Liu, X.; Zhang, S.; Gao, J.; Qian, Y. Growth of single-crystal Sb_2S_3 nanorods, dendrites and straw-tied-like architectures via a precursor−solvothermal−pyrolysis route. *J. Cryst. Growth* **2003**, *256*, 377−382.
(33) Hu, H.; Mo, M.; Yang, B.; Zhang, X.; Li, Q.; Yu, W.; Qian, Y. Solvothermal synthesis of Sb_2S_3 nanowires on a large scale. *J. Cryst. Growth* **2003**, *258*, 106−112.
(34) Zhang, H.; Hu, C.; Ding, Y.; Lin, Y. Synthesis of 1D Sb_2S_3 nanostructures and its application in visible-light-driven photodegradation for MO. *J. Alloys Compd.* **2015**, *625*, 90−94.
(35) Zhang, M.; Yoo, D.; Kang, Y.; Park, W.; Lee, J.; Kim, Y.; Hwang, Y.; Lee, D. Ni addition effects on physical properties of spin-coated Sb_2S_3 semiconducting compound thin films. *Appl. Surf. Sci.* **2023**, *607*, No. 155022.
(36) Zhang, M.; Park, W.; Kang, Y.; Yoo, D.; Kim, T.-H.; Lim, B.; Hwang, Y.-H.; Lee, D. Growth of single crystal Sb_2S_3 semiconductor pillars by sol-gel method. *Materialia* **2023**, *30*, No. 101842.
(37) Yu, S. H.; Yoshimura, M. Fabrication of Powders and Thin Films of Various Nickel Sulfides by Soft Solution-Processing Routes. *Adv. Funct. Mater.* **2002**, *12*, 277−285.
(38) Wang, Q.; Liu, F.; Wang, L.; Jiang, L.; Wang, Q.; Hong, B.; Lai, Y. Towards fast and low cost Sb_2S_3 anode preparation: A simple vapor transport deposition process by directly using antimony sulfide ore as raw material. *Scrip. Mater.* **2019**, *173*, 75−79.
(39) Makreski, P.; Petruševski, G.; Ugarković, S.; Jovanovski, G. Laser-induced transformation of stibnite (Sb_2S_3) and other structurally related salts. *Vib. Spectrosc.* **2013**, *68*, 177−182.
(40) Parize, R.; Cossuet, T.; Chaix-Pluchery, O.; Roussel, H.; Appert, E.; Consonni, V. In situ analysis of the crystallization process of Sb_2S_3 thin films by Raman scattering and X-ray diffraction. *Mater. Des.* **2017**, *121*, 1−10.
(41) Gale, W. F.; Totemeier, T. C. *Smithells Metals Reference Book*; Elsevier Butterworth-Heinemann, 2004.
(42) de Araújo, M. A.; Costa, M. B.; Mascaro, L. H. Improved Photoelectrochemical Hydrogen Gas Generation on Sb_2S_3 Films Modified with an Earth-Abundant MoS_x Co-Catalyst. *ACS Appl. Energy Mater.* **2022**, *5*, 1010−1022.
(43) Bard, A. J.; Faulkner, L. R. *Electrochemical Methods: Fundamentals and Applications*; John Wiley & Sons Inc, 2001.
(44) Tsege, E. L.; Atabaev, T. S.; Hossain, M. A.; Lee, D.; Kim, H.-K.; Hwang, Y.-H. Cu-doped flower-like hematite nanostructures for efficient water splitting applications. *J. Phys. Chem. Solids* **2016**, *98*, 283−289.
(45) Luo, P.; Zhang, H.; Liu, L.; Zhang, Y.; Deng, J.; Xu, C.; Hu, N.; Wang, Y. Targeted synthesis of unique nickel sulfide (NiS, NiS_2) microarchitectures and the applications for the enhanced water splitting system. *ACS Appl. Mater. Interfaces* **2017**, *9*, 2500−2508.

https://doi.org/10.1021/acs.jpcc.4c05586
J. Phys. Chem. C 2024, 128, 17463−17469